RSC Advances

PAPER

View Article Online
View Journal | View Issue

Cite this: *RSC Adv.*, 2015, **5**, 29698

One-pot synthesis of hierarchical WO_3 hollow nanospheres and their gas sensing properties

Chong Wang,[a] Changhao Feng,[a] Meng Wang,[a] Xin Li,[a] Pengfei Cheng,[b] Hong Zhang,[a] Yanfeng Sun,*[a] Peng Sun[a] and Geyu Lu*[a]

Received 20th January 2015
Accepted 17th March 2015

DOI: 10.1039/c5ra01121c

www.rsc.org/advances

In this paper, a one-pot synthesis of WO_3 hollow sphere nanostructure has been realized *via* a one-pot template-free solvothermal method. X-Ray diffraction patterns demonstrated that the products are pure monoclinic WO_3. Based on the observation of scanning electronic microscopy (SEM) and transmission electron microscopy (TEM), it was revealed that the as-prepared WO_3 nanospheres have a diameter of around 2 μm and are hollow structures with shell thickness of about 300 nm which are constructed by numerous oriented nanocrystals. Sensors based on the synthesized WO_3 hollow nanospheres exhibited high selectivity to NO_2 at low operating temperature. The detection limit can be as low as ~40 ppb level.

1. Introduction

Hollow nanostructures, in addition to their potential application in many fields,[1–4] would be very useful to improve gas-sensing properties because the rapid and effective diffusion of analyte gases onto the entire sensing surface.[5–7] Thus, it is of great interests to synthesize WO_3 nanocrystals with a hollow nanostructure. Up to now, various methods have been employed to obtain WO_3 crystals with a hollow nanostructure. Li *et al.* prepared WO_3 hollow spheres through the hydrolysis of tungsten hexachloride using novel carbon spheres as templates.[8] Chen *et al.* reported an acid-treated precursor method to synthesize WO_3 hollow nanostructures.[9] Yoon Ho Cho *et al.* prepared WO_3 hollow spheres using the ultrasonic spray pyrolysis method.[10] Among these methods, the complex operation is a negative factor to achieve the final hollow nanostructure. Therefore, a simple, effective and economical method is strongly desired to synthesize WO_3 hollow nanospheres.

As air pollution is becoming a serious issue, people have paid more attention to gas sensors and have achieved excellent work.[11,12] NO_2, as one kind of toxic gas, can affect human health even at parts per million (ppm) levels, such as in the respiratory system and nerve system.[13] In addition, it can also cause photochemical smog and acid.[14] The Occupational Safety and Health Administration (OSHA) have set a permissible exposure levels for NO_x at 5 ppm,[15] and the threshold concentration of NO_2 in air is 3 ppm as listed in the safety standards by the American Conference of Governmental Industrial Hygienists.[16] Thus, there is a strong demand for developing cheap, reliable and sensitive gas sensors targeting NO_2.[17] Therefore, the excellent response to NO_x makes WO_3 particularly outstanding for monitoring environment pollution and detecting leakage in industrial settings.[18,19] As a result, much attention has been paid to the synthesis of various nanostructured WO_3, such as nanowire,[20] nanoplate,[21] hollow nanosphere.[22] From the viewpoint of sensing, hollow nanospheres attract more interest as they can serve as effective transport channels and active sensing sites for analyte gas molecules, which are crucial for high response and fast response/recovery process.[23,24]

In this paper, we report a one-step template-free solvothermal route for the preparation of hierarchical hollow WO_3 nanosphere. This kind of facile chemical route meets the requirements mentioned above and WO_3 obtained in that way has promising application in gas sensor area. Characterizations and sensing properties are also reported here. The hollow nanostructures-based gas sensor showed high sensing performances toward NO_2 gas. The results are promising for further application of such hierarchical nanostructures as gas sensor.

2. Experimental

2.1. Synthesis and characterization of hollow nanosphered WO_3

All reagents (analytical-grade purity) were used without any further purification. In a typical synthesis, 1 g sodium tungstate and 1.2 g citric acid were dissolved in a mixture of distilled water (25 ml) and glycerol (10 ml). After stirring for 20 min, 4 ml 3 M HCl was added dropwise to the solution. Five minutes later, the above solution was transferred into a Teflon-lined stainless steel autoclave, sealed tightly, and maintained at 180 °C for 24 h. After the autoclave was allowed to cool to room temperature naturally, the precipitates were washed with deionized water and absolute ethanol for several times using a centrifuge, and

[a]*State Key Laboratory on Integrated Optoelectronics, College of Electronic Science and Engineering, Jilin University, Changchun 130012, People's Republic of China. E-mail: syf@jlu.edu.cn; lugy@jlu.edu.cn; Fax: +86 431 85167808; Tel: +86 431 85167808*
[b]*School of Aerospace Science and Technology, Xidian University, Xi'an 710126, People's Republic of China*

then dried at 80 °C for 24 h. The precipitates were calcined at 500 °C for 3 h with a heating rate of 5 °C min^{-1}. The calcined products were then collected for further analysis.

X-Ray power diffraction (XRD) analysis was conducted on a Rigaku D/max-2500 X-ray diffractometer with Cu Kα1 radiation (λ = 1.54056 Å) in the range of 20–60°. The morphology was examined by field-emission scanning electron microscopy (FESEM, JEOL JSM-7500F, operated at an acceleration voltage of 15 kV). Transmission electron microscopy (TEM), selected-area electron diffraction (SAED) were obtained on a JEOL JEM-2100 microscope operated at 200 kV.

2.2. Fabrication and measurement of sensor

The calcined powders were mixed with ethanol to form a paste which was then coated slowly and lightly onto an alumina tube (4 mm in length, 1.2 mm in external diameter and 0.8 mm in internal diameter) using a small brush. The tube was installed with a pair of gold electrodes, and each electrode was connected with two Pt wires. After brushing, a thick film was formed. After drying at room temperature, the sensing device was then sintered at 300 °C for 2 h in air. Finally, a Ni–Cr alloy coil was inserted into the alumina tube as a heater in order to control the operating temperature of the sensor. A schematic structure of the as-fabricated sensor was shown in Fig. 1a.

The electrical resistance of the sensor was measured in air and in target gas, respectively. The response of the sensor is defined as $S = R_g/R_a$ for oxidizing gas or R_a/R_g for reducing gas, here, R_a and R_g are the resistances of the sensor in the air and target gas, respectively. The response time and recovery time are defined as the time taken by the sensor to achieve 90% of the total resistance change during the adsorption and desorption processes, respectively. A schematic representation of the electric circuit is shown in Fig. 1b.

3. Results and discussion

3.1. Structural and morphological characteristics of the as-obtained WO_3

The typical XRD patterns of the products before and after sintering are shown in Fig. 2a and b. Both of the diffraction peaks can be well indexed to pure monoclinic WO_3 (JCPDS file no. 72-1465). No peaks of other impurity phases are detected from the patterns, indicating high purity of the product.

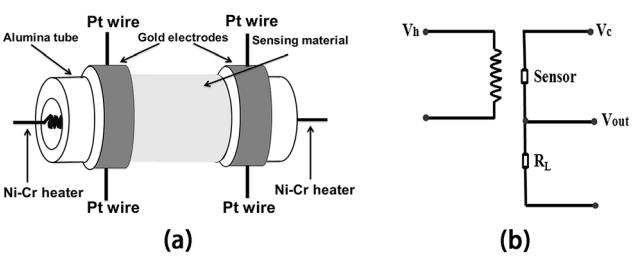

Fig. 1 (a) Schematic structure of the gas sensor. (b) Diagram of sensor and measurement electric circuit.

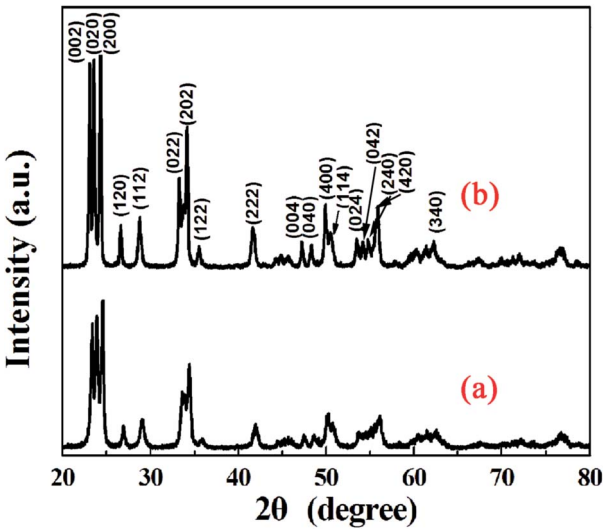

Fig. 2 X-Ray diffraction patterns of the sintered product before (a) and after sintering (b).

From a magnified SEM image (Fig. 3a), it can be seen that the sample possesses a hollow nanosphere structure with an average diameters of about 2 μm. Some microspheres with broken holes can also be observed and provide the direct evidence that the as-prepared WO_3 nanospheres are hollow in structure. An enlarged SEM image of a single cracked hollow nanosphere is presented in Fig. 3b, further confirming its

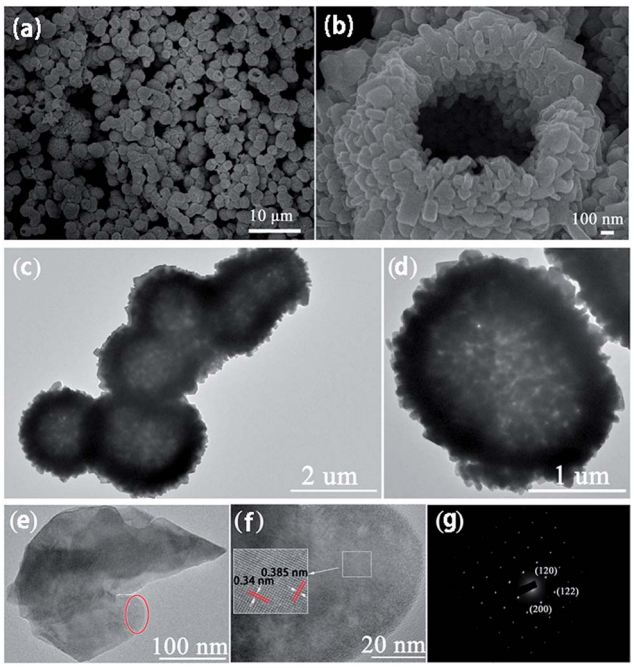

Fig. 3 (a and b) Typical SEM images of WO_3 product, (c) TEM images of the hierarchical WO_3 hollow nanospheres, (d) a typical nanosphere, (e) an individual nanosheet from the cracked nanosphere, (f) HRTEM image of a part of the nanosheet in (e), (g) the corresponding SAED patterns of the WO_3 nanosheet.

hollow structure. Furthermore, it displays that the shell of the hierarchically hollow spheres consists of organized WO_3 nanocrystals.

In addition, the WO_3 product was further characterized by TEM, and the corresponding TEM images are shown in Fig. 3c and d. The obvious contrast between the dark edge and the relatively bright center confirms its hollow nature. From a detailed inspection of Fig. 3d, it can be seen that the shell thickness is about 300 nm. The TEM image of an individual nanocrystal is shown in Fig. 3e. The HRTEM image of the part of the individual nanocrystal is presented in Fig. 3f. The clearly resolved lattice fringes in the HRTEM images confirmed the high crystallinity of the nanocrystal. The space between adjacent lattice planes along a certain direction is 0.34 nm, whereas the space between adjacent lattice planes along the other direction is 0.385 nm. They are found to correspond to (120) and (002) planes of monoclinic WO_3 crystal (JCPDS no. 72-1465), respectively. The Selected Area Electron Diffraction (SAED) patterns result is shown in Fig. 3g, which indicates that the nanocrystals of monoclinic WO_3 are single crystalline.

Nitrogen adsorption and desorption measurements were performed to evaluate the porosity and surface area of the as-synthesized WO_3 structures. The nitrogen adsorption and desorption isotherm plots and corresponding pore-size distribution plots of the hierarchical WO_3 hollow structures are given in Fig. 4. From the curves, we can see that this sample has two obvious peaks in the pore-size distribution plot at about 2.7 nm and 48.7 nm, respectively, and displays porous structures with a wide range of pore size distributions from 1.7 nm to 167 nm, which is beneficial for the target gas to adsorb on the sensing layer. The BET surface area of the product was calculated to be 5.4584 $m^2\ g^{-1}$.

To reveal the growth process of hollow nanosphered WO_3 and possible growth mechanism, a series of experiments using different reaction times were performed. When the reaction time was only 10 min, no precipitate was obtained. When the reaction time was increased to 15 min, some precipitates emerged and the morphology results are shown in Fig. 5a. 3D solid nanospheres with oriented nanosheets can be observed. The diameter of the spheres was about 1 μm. Following Gibbs law, the dissolved nanoparticles further aggregated onto the solid nanospheres through an oriented attachment in order to minimize the total surface energy, as shown in Fig. 5b. The diameter of the nanosphere became visibly bigger (~2 μm). When the reaction time was increased to 1 h, hollow structures appeared among the solid nanospheres (Fig. 5c). As the reaction time was extended to 24 h, all the solid nanospheres transformed into hierarchical hollow nanostructures (Fig. 5d). We believe that the evolution of morphology can be explained by the Ostwald ripening mechanism,[25,26] in which a classic phenomenon in particle growth involves the growth of larger particles at the cost of smaller particles due to the higher solubility of smaller particles. In the initial stages, solid nanoparticles as precursors are formed. With the consuming of the reactants, full nanospheres formed. With the reaction processed, the inner particles, which possess nanoscale diameters and higher surface energy, would dissolve and transfer to the outer space, finally forming the inner hollow nanostructures.

3.2. Gas-sensing properties for NO_2

Sensing properties of the sensor based on the hollow nanosphered WO_3 samples were investigated. It is well known that the response of a gas sensor is highly influenced by the operating temperature.[27] The correlation of the gas response of the sensor to 1 ppm NO_2 and the operating temperature was tested, and the results are shown in Fig. 6. As a comparison, a sensor based on commercial WO_3 was also measured. It is obvious that the hierarchical hollow nanostructures exhibited superior response over the commercial WO_3. It can be seen that the response increases with a raise of operating temperature and reaches the maximum value at 100 °C. When the temperature is further increased, the response decreases gradually, indicating that the response is greatly influenced by temperature.

This phenomenon can be explained as follows: the increase of the response can be attributed to an increase of the surface reaction ($NO_{2(g)} + e^- \rightarrow NO_{2(ads)}^-$). Such adsorption can capture the electrons from WO_3 resulting in an increase of the electrical resistance. However, when the temperature is higher, a larger number of oxygen molecules dissociate and adsorb on the active sites, resulting in a decrease of the free active sites for the adsorption of NO_2. On the other hand, the rate of adsorption is lower than desorption at such higher temperatures.[25,28,29]

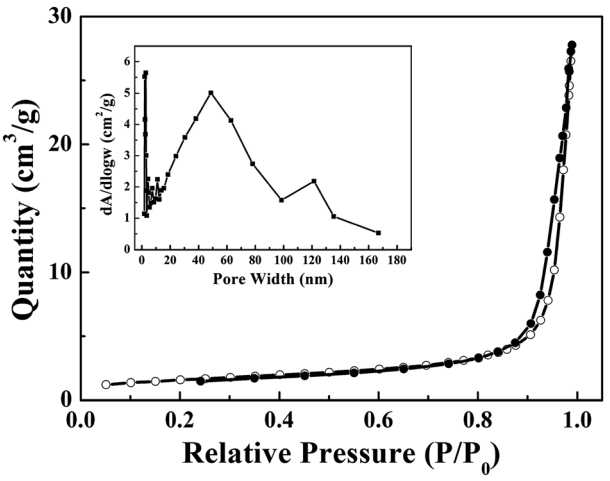

Fig. 4 Nitrogen adsorption–desorption isotherm and corresponding pore-size distribution of as-synthesized WO_3 sample.

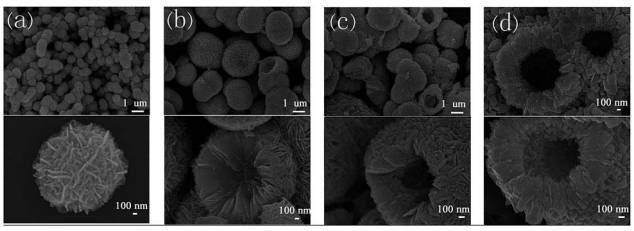

Fig. 5 FESEM images of the morphology evolution at different reaction times: (a) 15 min, (b) 45 min, (c) 1 h and (d) 24 h.

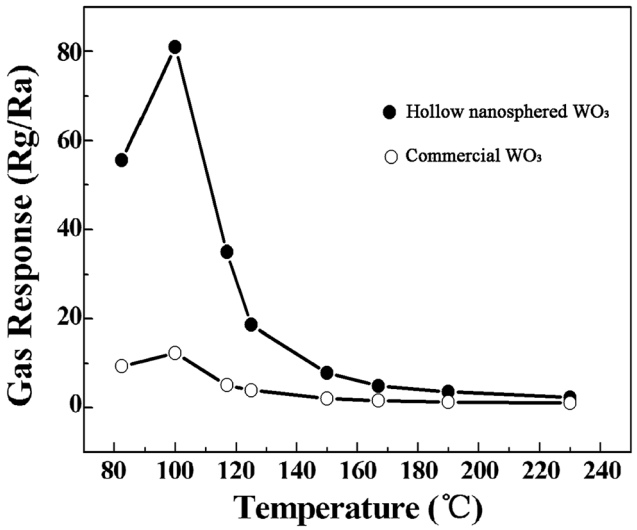

Fig. 6 Correlations between the gas response to 1 ppm NO_2 and the operating temperature for hollow nanosphered WO_3 and commercial WO_3.

Therefore, 100 °C was chosen as the optimum working temperature of the sensor. The four reversible cycles of the response curve indicate a stable and repeatable characteristic, as shown in the inset of Fig. 7; the response time and recovery time were about 237 s and 88 s, respectively. Fig. 8a displays the response/recovery curves of the sensors to NO_2 with concentrations varying from 40 to 4000 ppb at the optimum operating temperature. The resistance of the sensor increases upon exposure to NO_2, whereas it decreases upon removal of NO_2. The response of the sensor increased with an increase of gas concentration. The profile of the sensor response as a function of NO_2 gas concentrations is shown in Fig. 8b. It is interesting to note that the response of the sensor to 40 ppb NO_2 is about 3.4, which demonstrates that the sensor exhibits an acceptable response from a practical viewpoint. A comparison of the

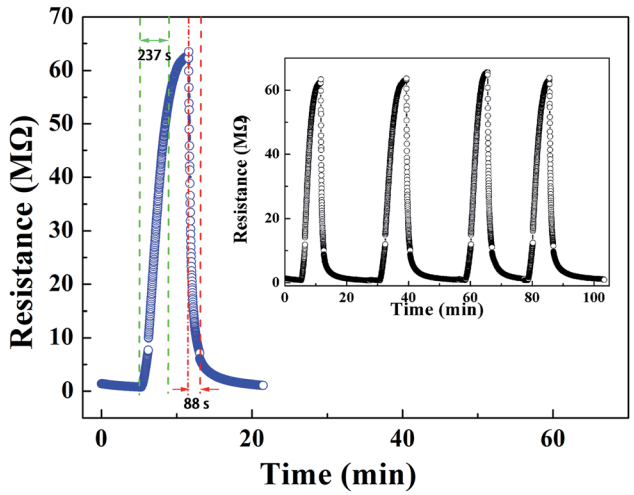

Fig. 7 Four periods of response curve to 1 ppm NO_2 at 100 °C.

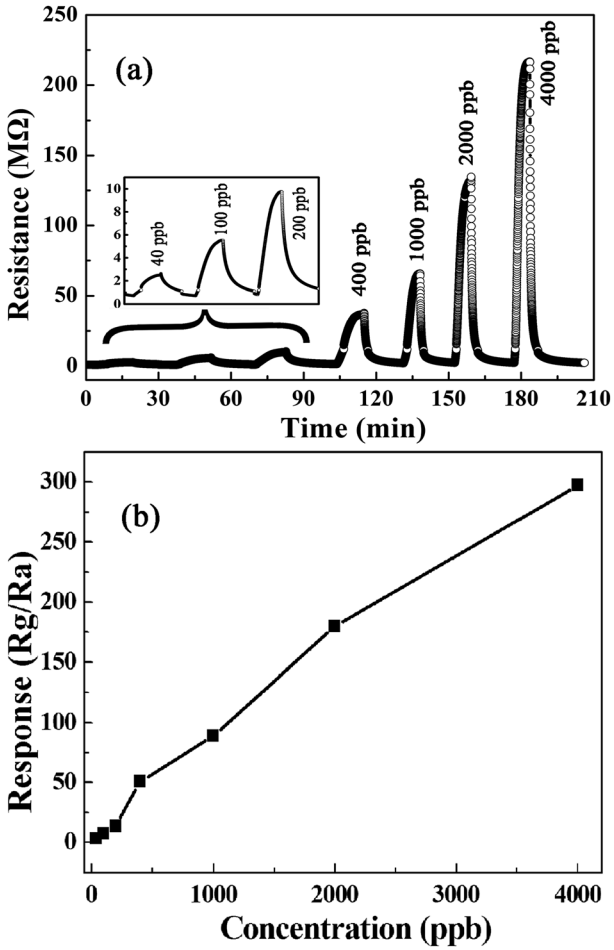

Fig. 8 (a) Response transients of the sensor to different NO_2 concentration at 100 °C. (b) Gas response of the sensor as a function of NO_2 concentrations.

sensing performances between the sensor fabricated in this work and literature reports is summarized in Table 1. From the table, it can be seen that the sensor based on WO_3 hollow nanospheres has a correspondingly high gas response and low working temperature. These results demonstrate that the hollow nanosphered WO_3-based sensor has a quite high response to NO_2 and a relative low working temperature.

The long-term stability of the gas sensor is a relative crucial parameter from a practical viewpoint. The response as a function of the number of testing days was also measured and shown in Fig. 9. The response of the sensor to 1 ppm NO_2 at 100 °C was nearly constant over two weeks, which indicated the splendid long-term stability of the sensor based on WO_3 hollow nanospheres.

WO_3 is a typical n-type semiconductor, and its gas-sensing mechanism belongs to the surface-controlled type. In air ambient, oxygen molecules are adsorbed onto the surface of the as-synthesized WO_3 and generate the chemisorbed oxygen species (O_2^-, O^- and O^{2-}) by capturing electrons from the conduction band of WO_3, depletion region is formed on the surface area of WO_3.[27] Upon exposure to NO_2 gas, the NO_2 gas

Table 1 Gas responses to NO_2 in the present study and those reported in the literatures

Material	Preparation	NO_2 concentration	Operating temperature	Response	Ref.
WO_3	Hydrothermal	1 ppm	100 °C	89	Present study
WO_3	Hydrothermal	1 ppm	300 °C	54	22
WO_3	Ultrasonic spray pyrolysis	1 ppm	300 °C	4.8	10
WO_3	Hydrothermal	1 ppm	300 °C	5.3	25

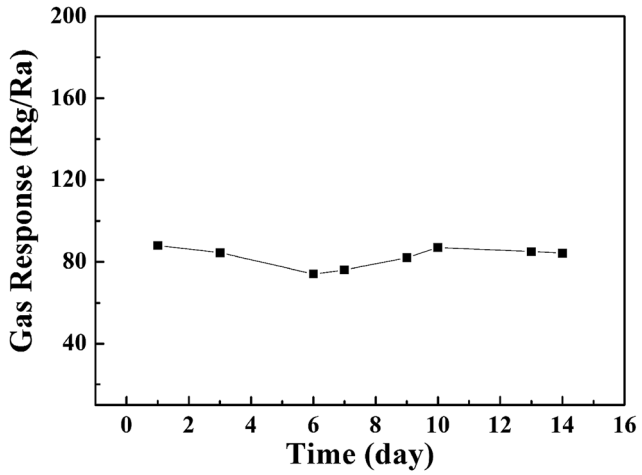

Fig. 9 Stability of the sensor based on as-prepared sample at 100 °C.

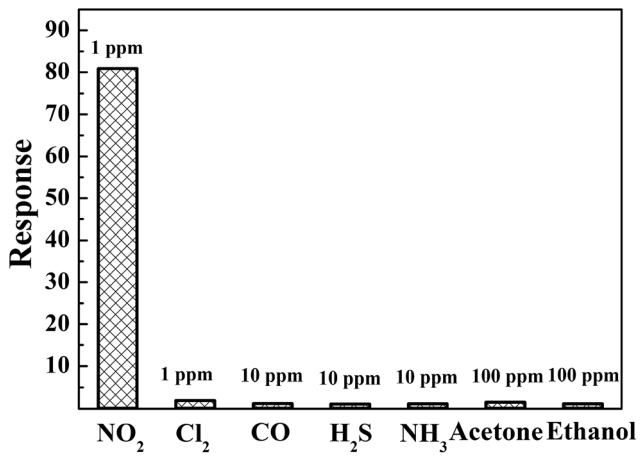

Fig. 10 Comparison of responses of the sensor based on WO_3 to various gases at 100 °C.

molecules are directly absorbed on the active sites on tungsten oxide surface. Charge transfer is likely to occur from WO_3 to absorbed NO_2 because of the strong electron-withdrawing power of the NO_2 molecules, resulting in a large increase in electrical resistance. The special hierarchical hollow nanosphere structure, which is beneficial for the rapid and effective diffusion of analyte gases onto the entire sensing material, might be the reasons for the high response of the sensor to NO_2. Therefore, the sensor is expected to have high response to NO_2.

It is well known that selectivity is another important parameter of a sensor with a view of practical application. Therefore, at the optimum operating temperature, the response of the sensor based on the hierarchical hollow nanosphere to various kinds of gases was investigated, such as Cl_2, CO, H_2S, NH_3, acetone and ethanol, as shown in Fig. 10. It can be seen that the sensor has a high response to NO_2 compared to the other gases. Such result demonstrates that the sensor using the WO_3 nanostructure synthesized here exhibits an excellent selectivity to NO_2 against the other tested gases at the working temperature of 100 °C.

4. Conclusion

In summary, hierarchical WO_3 hollow nanosphere has been successfully synthesized through a simple one-step solution route. Field emission scanning electron microscopic and transmission electron microscopy results demonstrate that the products are composed of numerous nanocrystals. In addition, gas sensing properties of sensors based on the hollow WO_3 nanospheres toward NO_2 were investigated. The sensor exhibits excellent NO_2 sensing properties at 100 °C. These results indicate that our sensor might have potential application to fabricate highly sensitive NO_2 gas sensor devices.

Acknowledgements

This work is supported by Application and Basic Research of Jilin Province (20130102010JC), the National Nature Science Foundation of China (no. 61304242, 61327804, 61134010, 61377058 and 61374218), Program for Chang Jiang Scholars and Innovative Research Team in University (no. IRT13018) and "863" High Technology Project (2013AA030902), China Scholarship Council.

References

1 H. Huang and E. E. Remsen, *J. Am. Chem. Soc.*, 1999, **121**, 3805–3806.
2 W. Meier, *Chem. Soc. Rev.*, 2000, **29**, 295–303.
3 P. F. Cheng, P. Sun, S. S. Du, Y. X. Cai, X. W. Li, Z. Wang, F. M. Liu, J. Zheng and G. Y. Lu, *RSC Adv.*, 2014, **4**, 23396–23404.
4 X. W. Li, W. Feng, Y. Xiao, P. Sun, X. L. Hu, K. Shimanoe, G. Lu and N. Yamazoe, *RSC Adv.*, 2014, **4**, 28005–28010.
5 N. Du, H. Zhang, B. D. Chen, X. Y. Ma, Z. H. Liu, J. B. Wu and D. R. Yang, *Adv. Mater.*, 2007, **19**, 1641–1645.

6 H. G. Zhang, Q. S. Zhu, Y. Zhang, Y. Wang, L. Zhao and B. Yu, *Adv. Funct. Mater.*, 2007, **17**, 2766–2771.
7 M. Tiemann, *Chem.–Eur. J.*, 2007, **13**, 8376–8388.
8 X. L. Li, T. J. Lou, X. M. Sun and Y. D. Li, *Inorg. Chem.*, 2004, **43**, 5442–5449.
9 D. Chen and J. H. Ye, *Adv. Funct. Mater.*, 2008, **18**, 1922–1928.
10 Y. H. Cho, Y. C. Kang and J. H. Lee, *Sens. Actuators, B*, 2013, **176**, 971–977.
11 S. Agarwala, W. L. Ong and G. W. Ho, *Sci. Adv. Mater.*, 2013, **5**, 1418–1426.
12 S. Agarwala, Z. H. Lim, E. Nicholson and G. W. Ho, *Nanoscale*, 2012, **4**, 194–205.
13 B. T. Marquis and J. F. Vetelino, *Sens. Actuators, B*, 2001, **77**, 100–110.
14 G. Eranna, B. C. Joshi, D. P. Runthala and R. P. Gupta, *Crit. Rev. Solid State Mater. Sci.*, 2004, **29**, 111–188.
15 OSHA and MSHA Diesel Exposure Limit, 2006.
16 M. Penza, C. Martucci and G. Cassano, *Sens. Actuators, B*, 1998, **50**, 52–59.
17 Y. Shimizu, H. Nishi, H. Suzuki and K. Maeda, *Sens. Actuators, B*, 2000, **65**, 141–143.
18 B. Deb, S. Desai, G. U. Sumanasekera and M. K. Sunkara, *Nanotechnology*, 2007, **18**, 285501.
19 C. Cantalini, H. T. Sun, M. Faccio, M. Pelino, S. Santucci, L. Lozzi and M. Passacantando, *Sens. Actuators, B*, 1996, **31**, 81–87.
20 Y. M. Zhao and Y. Q. Zhu, *Sens. Actuators, B*, 2009, **137**, 27–31.
21 K. F. Wang, P. F. Zeng, J. Zhai and Q. Q. Liu, *Electrochem. Commun.*, 2013, **26**, 5–9.
22 C. Y. Lee, S. J. Kim, I. S. Hwang and J. H. Lee, *Sens. Actuators, B*, 2009, **142**, 236–242.
23 J. H. Lee, *Sens. Actuators, B*, 2009, **140**, 319–3369.
24 D. W. Wang, S. S. Du, X. Zhou, B. Wang, J. Ma, P. Sun, Y. F. Sun and G. Y. Lu, *CrystEngComm*, 2013, **15**, 7438.
25 X. Q. An, J. C. Yu, Y. Wang, Y. M. Hu, X. L. Yu and G. J. Zhang, *J. Mater. Chem.*, 2012, **22**, 8525–8531.
26 W. Z. Ostwald, *Phys. Chem.*, 1897, **22**, 289.
27 N. Yamazoe, G. Sakai and K. Shimanoe, *Catal. Surv. Asia*, 2003, **7**, 63–75.
28 B. Ruhland, T. Becker and G. Müller, *Sens. Actuators, B*, 1998, **50**, 85–94.
29 A. P. Lee and B. J. Reedy, *Sens. Actuators, B*, 1999, **60**, 35–42.